Dynamic characterization, flow modelling, and hierarchical control of an energy-harvesting underwater kite in realistic ocean conditions

James Reed, Michael Muglia, Mitchell Cobb, and Chris Vermillion

Abstract—**This paper presents a hierarchical control framework for a kite-based marine hydrokinetic (MHK) system, along with a detailed characterization of the dynamic and energetic performance of the system under realistic flow conditions. The underwater kite, which is designed to be deployed off of an offshore floating platform, features a closed-loop controller that executes power-augmenting, cyclic cross-current flight. The robustness of the kite's undersea flight control algorithm is demonstrated in a realistic four-dimensional flow model (which captures both low-and high-frequency spatiotemporal variations in the current) that accounts for turbulence and wave effects, which is coupled with a detailed dynamic model that captures the six-degree-of-freedom kite and floating platform dynamics, in addition to the tether dynamics. Using data obtained by the Coastal Data Information Program (CDIP) 192 Oregon Inlet buoy, wave data from the Wave Information Studies Hindcast model, and a spectral turbulence model developed at Florida Atlantic University, we demonstrate the robustness of the kite's control system and the sensitivity of both average net power output and peak-to-average power to wave parameters. In common wave conditions, the average and net power output are shown to be highly robust to the peak period and significant wave height. In extreme wave conditions, the peak-to-average power ratio is shown to be highly positively correlated with an *effective wave energy density* metric, which characterizes the wave energy density presented to the kite system based on a weighted distribution along depth of the kite.**

Index Terms—**Energy-Harvesting Kites, Hierarchical Control, Marine Hydrokinetic Energy, Ocean Current Modeling**

I. INTRODUCTION

MARINE hydrokinetic (MHK) resources have been estimated to possess as much as 1229 TWh/year of wave energy [1], 334 TWh/year of usable tidal energy [2], and 163 TWh/year of usable ocean current energy [3] within the United States alone. This collective MHK resource is sufficient to power tens of millions of homes, in addition to powering oceanographic research buoys, navigational buoys, autonomous underwater vehicles, and other entities that comprise the so-called "blue economy" [4]. However, economically practical extraction of MHK resources is complicated by the large required size of such devices (for example, a fixed ocean turbine operating in a 1 m/s flow speed must be approximately as large per unit power as a towered wind energy system operating in a 10 m/s wind speed, yet the costs of building such a device underwater are much larger) and the locations in which these resources exist (for example, the strongest portion of the Gulf Stream routinely lies in waters that are at least 1 km deep, as noted in [5]).

Underwater kites represent a relatively new technology for harvesting tidal and current resources using an order of magnitude less material than fixed turbines. Depicted in Fig. 1, a kite-based MHK system consists of a rigid wing that is tethered to either the seabed or a surface platform and flown in a pattern *perpendicular* to the prevailing current. Energy can be generated either through on-board rotors [6] or through cyclic spooling motion [7], whereby tether is spooled out under high tension and spooled in under low tension, resulting in net positive energy generation at a winch located on the seabed/platform. As shown in [8], for a high lift/drag wing, this *cross-current* motion can easily result in more than an order of magnitude more power than that of a stationary system of the same size. A free-body diagram for this concept can be seen in Fig. 2, with example tethered MHK system designs shown in Fig. 3. The ability to achieve such high power density has led to the popularization of kite-based systems not only for harvesting MHK resources, but also in the sister field of airborne wind energy, as practiced by companies like Windlift, Inc. [9], SkySails Power [10], and Kitemill [11].

This work will focus specifically on an MHK kite design that generates net energy through cyclic spooling motion, which can in general be accomplished in one of two ways, or a combination thereof:

1) *multi-cycle spooling*, where tether is continually spooled out under high tension over multiple laps during cross-current flight (where a lap is

This paper was submitted for review on 5 August, 2021, revised 22 November 2022, accepted 19 December 2023. This research is supported by the Department of Energy, award number DE-EE0008635 and the National Science Foundation Graduate Research Fellowships Program.

James Reed is with the Department of Mechanical and Aerospace Engineering at North Carolina State University, 911 Oval Dr, Raleigh, NC 27606, USA (e-mail: jcreed2@ncsu.edu).

Michael Muglia is with the Coastal Studies Institute of East Carolina University, 850 NC-345, Wanchese, NC 27981, USA (e-mail: mugliam@ecu.edu).

Mitchell Cobb is with Blue Origin, 21601 76th Ave S, Kent, WA 98032, USA (e-mail: mcobb@ncsu.edu).

Chris Vermillion is with the Department of Mechanical and Aerospace Engineering at North Carolina State University, 911 Oval Dr, Raleigh, NC 27606, USA (e-mail: cvermil@ncsu.edu).

Digital Object Identifier: https://doi.org/10.36688/imej.6.91-107

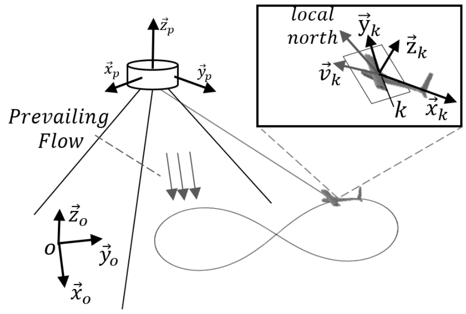

Fig. 1: Concept of operations for cross-current figure-8 flight as deployed from a floating platform.

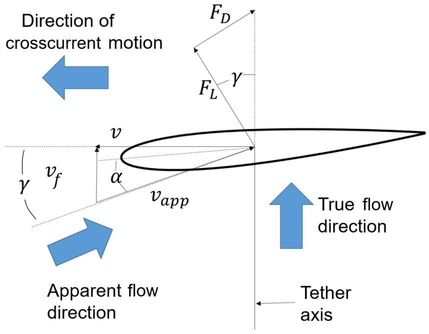

Fig. 2: Free-body diagram of a hydrofoil undergoing crosscurrent flight. Nomenclature: v = kite velocity, v_f = flow velocity, v_{app} = apparent flow velocity, F_L = lift force, F_D = drag force, α = angle of attack.

one complete traversal of a path), and spooled in under low tension either radially towards the base station or in a path-following configuration under low-tension, low-lift flight; or

2) *intra-cycle spooling*, where the spooling rate is adjusted over the course of each lap, spooling tether out at high angles of attack on portions of the path corresponding to high tension, and spooling tether in at low angles of attack on portions of the path corresponding to low tension.

Several studies, including [7], [12], [13], and [14], have presented hydrodynamic characterizations, dynamic models, and corresponding controllers for MHK kites. In [7], a kite system was numerically simulated in a constant flow environment. In [12], a kite system was numerically simulated in a constant flow environment, and a hydrodynamic characterization of the kite was performed. The key results of [7] and [12] are the development of a two-dimensional simulation model for underwater kite systems and a study showing baseline power predictions for the two-dimensional kite system. In [13], a dynamic model and controller were developed for an underwater kite system in a constant flow environment. Finally, in [14], a multi-degree-of-freedom Lagrangian dynamic model and corresponding proportional plus derivative (PD) feedback controller were developed. In both [13] and [14], using the derived dynamic models and controllers, power predictions were made for the kite system using a simplified turbine model to predict power. While these works provide meaningful modeling contributions, the results are restricted to spatiotemporally uniform flow environments. Thus, additional questions remain regarding how well the MHK kite control systems will perform, in terms of robustness and power production, in realistic ocean environments that consist of low-frequency spatiotemporal flow variations, high-frequency turbulence, and (when deployed off of floating platforms or in sufficiently shallow waters) wave effects. While performance in turbulent conditions has been studied in the sister field of kite-based *wind* energy systems (for example, in [15] and [16]), in addition to the field of *stationary* MHK systems in [17] and [18], the dissimilar time and length scales of ocean currents, in addition to the different system dynamics of kites vs. stationary systems, motivate kite-specific studies in realistic ocean environments.

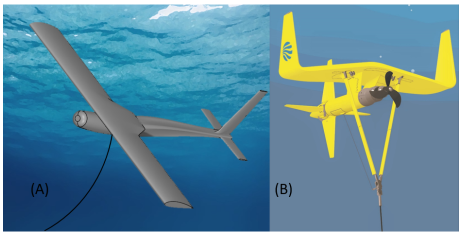

Fig. 3: The above figure shows the kite design used in this work in subfigure (A), and an example system used by Minesto Ltd. in subfigure (B).

Our previous work in [19] presented a hierarchical flight control system and intra-cycle spooling controller for an MHK kite, which was shown to be robust in the presence of a realistic turbulent flow environment. While the work in [19] represented an ideal starting point for modeling an energy-harvesting kite system deployed in a realistic ocean environment, it does not consider the actual platform that the kite would be deployed off of, nor does it consider the effects of waves on the kite system or platform. Additionally, while the work in [19] presents projected lap-averaged power output (i.e., averaged over a figure-8 cycle), it does not consider the peak-to-average power ratio, which is understood to be a very important techno-economic metric that drives structural and power take-off (PTO) design considerations.

In augmenting our modeling framework from [19] with a floating platform off of which the kite is deployed, we sought to strike a balance between model fidelity and simplicity. In the realm of floating platform dynamic modeling, [20], [21], and [22] are some of the many works that analyze the dynamics of the floating bodies using finite element methods. While highly accurate, the mathematical and computational complexity of these models render them unsuitable for either control design or rapid simulation. An attractive approach shown in [23] uses a lumped body model that allows the forces and moments to be calculated for each lumped body. While their implementation is built on top of Orcaflex software, we incorporate the underlying mathematics of their lumped body model into our own custom integrated model (which integrates the floating platform, the tether, and the kite), where the forces and moments are computed and summed over all lumped masses, and the platform is ultimately characterized as a six-degree-of-freedom rigid body. In order to smooth discontinuities that would otherwise exist in the model due to the discrete number of lumped masses, each lumped mass is assigned a radius, and hydrodynamic and buoyant forces on each node are computed based on the fraction of the lumped mass that is submerged.

In addition to the aforementioned floating platform model, our modeling framework also considers surface waves, and their impact on the flow velocity field below the surface. While many complex nonlinear wave modeling approaches exist, such as 5th order Stokes' theory and Fourier approximation wave theory, we chose to model ocean waves using plane progressive waves, as described in [24]. The plane progressive formulation strikes an ideal balance between model simplicity (needed for control system development and rapid simulation) and accuracy; in particular, the plane progressive modeling formulation allows us to perform a detailed characterization of kite performance over a representative range of wave amplitudes and periods.

As noted before, our previous work in [19] presented a hierarchical flight control system and intra-cycle spooling controller for an MHK kite, which was shown to be robust in the presence of a realistic turbulence environment. This work expands upon our previous work by:

- Incorporating a six-degree-of-freedom floating platform model with lumped mass non-compressive spring-damper mooring lines;
- adding ocean waves characterized by observed wave parameters from the Coastal Data Information Program (CDIP) 192 Oregon Inlet buoy [25] and wave parameters taken from the Wave Information Studies hindcast model [26], making this the most comprehensive ocean current modeling environment to-date for energy-harvesting kite dynamic simulations;
- characterizing closed-loop flight performance of a candidate kite design operating from a floating platform, considering two candidate platform sizes, the presence of spectral turbulence, and a wide array of wave parameters; and
- performing a detailed analysis of the impact of wave energy on lap-averaged power output and peak-to-average power output, using an *effective energy density* metric that characterizes the impact of wave propagation along the entire tether length.

The results of our analysis show that the proposed kite and corresponding controller will deliver robust performance, both in terms of flight performance and lap-averaged power output, over a full range of wave conditions, in the presence of high-frequency turbulence, with different platform sizes. Further analysis demonstrates that in common wave conditions, the average and net power output are shown to be highly robust to the peak period and significant wave height. In extreme wave conditions, the peak-to-average power ratio is shown to be highly positively correlated with the effective wave energy density injected into the system when the kite is deployed from an infinitely large platform, and when the kite is deployed from a small platform, the variability in the peak-to-average power ratio is shown to increase as well as being positively correlated with the effective wave energy density.

II. Plant Model

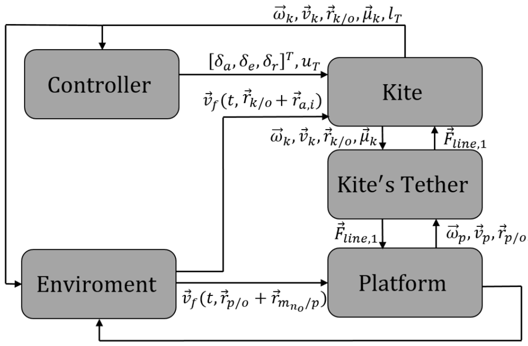

Fig. 4: The above figure shows complete system model, and the information that is exchanged between each component.

Following our earlier work in [27], the MHK kite is modeled as a combination of a rigid lifting body wherein forces and moments are calculated from lift, drag, buoyancy, and gravity, and a lumped mass tether model whose links are characterized as non-compressive spring-damper systems, as in [28]. The dynamics of the kite in this paper are reformulated using the method prescribed by [29] to allow for the inclusion of added mass terms. The instantaneous mechanical power produced by the system $P_{gen}(t)$, is modeled as:

$$P_{gen}(t) = ||\vec{F}_{Line,1}|| \tilde{u}_T(t), \tag{1}$$

where $\tilde{u}_T(t)$ is the spool speed of the tether, and $\vec{F}_{Line,1}$ is the force from the kite's tether. This work expands upon our previous work in [19] with the inclusion of an anchored, lumped mass floating platform that the kite is deployed off of. The mooring lines of the floating platform are modeled in the same fashion as the kite's tether, but with different representative parameter values.

In Figure 4, the components of the overall model are shown as well as the signals exchanged between them. In the figure, $\vec{\omega_k}, \vec{v}_k, \vec{r}_{k/o}, \vec{\mu}_k$, and l_T correspond to the kite's angular velocity, the kite's velocity, the kite's position, the kite's orientation, and the kite's un-spooled tether length, $\vec{\omega_p}, \vec{v}_p, \vec{r}_{p/o}$, and $\vec{\mu}_p$ corresponds to the platform's angular velocity, the platform's velocity, the platform's position, and the platform's orientation. Additionally, $[\delta_a, \delta_e, \delta_r]^T$ correspond to the kite's control surface deflections, u_T corresponds to the spooling speed commanded to the winch (which is inside of the block labeled "kite"), $\vec{v}_f(t, \vec{r}_{k/o} + \vec{r}_{a_i})$ are the flow vectors at the hydrodynamic surfaces of the kite, and $\vec{v}_f(t, \vec{r}_{p/o} + \vec{r}_{m_{n_o}/p})$ are the flow vectors at the outer lumped masses of the platform. The flow environment and controller blocks are discussed in detail in Sections III and IV.

In this work, in modeling waves and wave forces, the deep-water wave assumption is used [24], which is valid when the seabed depth at the locations used is greater than half of the wave's wavelengths.

A. Lifting Body (Kite) Model

As indicated in Fig. 5, the coordinate system used for the kite is described by three body-fixed orthonormal unit vectors, $\vec{x}_k$, $\vec{y}_k$, and $\vec{z}_k$, whose origin lies at the kite's center of mass. An additional ground-frame coordinate system is described by orthonormal unit vectors $\vec{x}_o$, $\vec{y}_o$, and $\vec{z}_o$, also indicated in Fig. 5. The state variables describing the position and orientation (and rates of change of the position and orientation) of the kite evolve according to the nonlinear equations of motion:

$$\dot{\mathbf{v}}_r = \mathrm{M_k}^{-1}\left(\tau(\mathbf{v}_r) - \mathbf{C}\left(\mathbf{v}_r\right)\mathbf{v}_r\right), \tag{2}$$

where

$$\mathbf{v}_r = \begin{bmatrix} u_{\text{kite}} - u_f \\ v_{\text{kite}} - v_f \\ w_{\text{kite}} - w_f \\ p \\ q \\ r \end{bmatrix}. \tag{3}$$

The variables u_{kite}, v_{kite}, and w_{kite} are the components of the kite's velocity aligned with the axes of k frame, and u_f, v_f, and w_f are the components of the flow velocity aligned with the k frame. Additionally, p, q, and r are the rotational rates about the kite's body axes, and are calculated by:

$$\begin{bmatrix} p \\ q \\ r \end{bmatrix} = \begin{bmatrix} \omega_{x,k} + \omega_{y,k}\sin\left(\phi_k\right)\tan\left(\theta_k\right) + \omega_{z,k}\cos\left(\phi_k\right)\tan\left(\theta_k\right) \\ \omega_{x,k}\cos\left(\phi_k\right) - \omega_{z,k}\sin\left(\phi_k\right) \\ \left(\omega_{y,k}\sin\left(\phi_k\right) + \omega_{z,k}\cos\left(\phi_k\right)\right)\sec\left(\theta_k\right) \end{bmatrix}, \tag{4}$$

where the components of angular velocity in the kite's body frame are given by:

$$\vec{\omega_k} \triangleq \left[\ \omega_{x,k} \quad \omega_{y,k} \quad \omega_{z,k}\ \right]^T. \tag{5}$$

The collection of Tait-Bryan angles describing this system are $\vec{\mu_k} \triangleq \left[\ \phi_k \quad \theta_k \quad \psi_k\ \right]^T$. This is the vector of roll (ϕ_k), pitch (θ_k), and yaw (ψ_k) Euler angles.

The vector τ is comprised of the external forces and moments and is given by:

$$\tau = \begin{bmatrix} \vec{F}_{Net,k} \\ \vec{M}_{Net,k} \end{bmatrix} \tag{6}$$

where $\vec{F}_{Net,k} \in \mathbb{R}^3$ is the vector containing the external forces on the kite, and $\vec{M}_{Net,k} \in \mathbb{R}^3$ is the vector containing the external moments on the kite. These include fluid dynamic forces and moments, which depend on $\mathbf{v}_r$, gravitational/buoyant forces (and associated moments), and the external force (and associated moment) from the tether. Additionally, $\mathbf{C}\left(\mathbf{v}_r\right) \in \mathbb{R}^{6\times6}$ is the matrix accounting for the Coriolis and centripetal terms arising from rigid body and added mass effects.

Finally, the matrix $\mathrm{M_k} \in \mathbb{R}^{6\times6}$ is the mass matrix of the kite, which is a combination of mass and inertia terms, coupling terms due to the body frame origin not being at the kite's center of mass, and added mass terms calculated based on the kite's geometry. Readers are referred to [29] for further details regarding the calculation of the matrices $\mathrm{M_k}$ and $\mathbf{C}\left(\mathbf{v}_r\right)$.

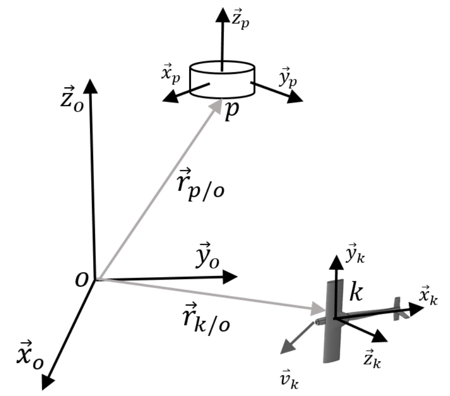

Fig. 5: The above figure shows the position vectors of both the floating platform and the kite. This figure also includes the ground-frame, kite body-frame, and platform body frame coordinate systems.

The kite is subjected to forces and moments arising from five surfaces (a fuselage, port wing, starboard wing, horizontal stabilizer and vertical stabilizer), buoyancy, gravity, and the tether. These forces and moments are calculated as:

$$\begin{aligned} \vec{F}_{Net,k} =& \vec{F}_{Line,1} + \left(V\rho - m\right)g\vec{z}_o \\ &+ \frac{1}{2}\rho A_r \sum_{i=1}^{5} \|\vec{v}_{a_i}\|^2 \left(C_{L,i}\vec{u}_{L,i} + C_{D,i}\vec{u}_{D,i}\right) \end{aligned} \tag{7}$$

where in (7), the first term is the force exerted at the center of mass (CM) of the kite by the tether on the lifting body, the second term describes the net buoyant force, and the last term describes the fluid dynamic forces. Here, V is the volume of the kite, ρ is the fluid density, m is the mass of the system, and g is the acceleration due to gravity.

The net moment applied to the system, $\vec{M}_{Net,k}$, is then calculated as the sum of the cross products of the individual fluid dynamic forces, as described by the last term in (7), and the appropriate associated moment arm, r_{a_i}:

$$\vec{M}_{Net,k} = \sum_{i=1}^{5} \vec{r}_{a_i} \times \frac{1}{2}\rho A_r \|\vec{v}_{a_i}\|^2 \left(C_{L,i}\vec{u}_{L,i} + C_{D,i}\vec{u}_{D,i}\right). \tag{8}$$

The index, i, refers to each of the five aforementioned surfaces. The force on each surface depends on the apparent flow at the hydrodynamic center of that particular surface, $\vec{v}_{a_i}$, which is calculated as:

$$\vec{v}_{a_i} = \vec{v}_f(t, \vec{r}_{k/o} + \vec{r}_{a_i}) - \left(\vec{v_k} + \omega \times \vec{r}_{a_i}\right), \tag{9}$$

where $\vec{v}_f(\cdot, t)$ is the spatially-varying flow profile, $\vec{v}_k$ is the kite's velocity, and $\vec{r}_{a_i}$ is the vector from the CM of the kite to the fluid dynamic center of the i^{th} surface. The fluid dynamic coefficients of (7) and (8), $C_{(L,D),i}(\vec{v}_{a_i})$, are obtained by modeling each fluid dynamic surface independently in the Athena Vortex Lattice (AVL) software created by [30] and parameterizing them as functions of the associated control surface deflections, δ_i, as:

$$\begin{aligned} C_{(L,D),i}(\vec{v}_{a_i}) \quad = \quad & C_{(L_0,D_0),i}(\vec{v}_{a_i}) + C_{(L_1,D_1),i}\delta_i \\ & + C_{(L_2,D_2),i}\delta_i^2 \end{aligned} \tag{10}$$

where the control sensitivity coefficients, $C_{L_1,i}$, $C_{L_2,i}$, $C_{D_1,i}$, and $C_{D_2,i}$ were obtained from AVL. The spanwise lift coefficient distributions, $C_{l,i}(y)$, obtained from the software, were heuristically corrected to account for nonlinear stall behavior that is not present in AVL. This correction, $C_{L_0,i}$, is given by:

$$C_{L_0,i} = \sum_{j=1}^{N_c} \begin{cases} C_{l,i}(y_{j,i}), & C_{l,i}(y_{j,i}) < C_{l_{max}}(y_{j,i}) \\ 2C_{l_{max},i}(y_{j,i}) \\ \quad - C_{l,i}(y_{j,i}), & C_{l,i}(y_{j,i}) \geq C_{l_{max}}(y_{j,i}) \end{cases} \tag{11}$$

where N_c is the number of control points used in the AVL analysis, $y_{j,i}$ is the spanwise location of the j^{th} control point of surface i, and $C_{l_{max}}(y_{j,i})$ is the maximum hydrofoil lift coefficient at the j^{th} control point of surface i.

Finally, the variables $\vec{u}_{D,i}$ and $\vec{u}_{L,i}$ represent unit vectors describing the direction of the lift and drag forces at the i^{th} hydrodynamic center:

$$\vec{u}_{D,i} = \frac{\vec{v}_{a_i}}{\|\vec{v}_{a_i}\|}, \tag{12}$$

$$\vec{u}_{L,i} = \begin{cases} \begin{bmatrix} 0 & 0 & -1 \\ 0 & 0 & 0 \\ 1 & 0 & 0 \end{bmatrix} \dfrac{\left[\vec{u}^{x}_{D,i}\; 0\; \vec{u}^{z}_{D,i}\right]^T}{\|\left[\vec{u}^{x}_{D,i}\; 0\; \vec{u}^{z}_{D,i}\right]\|} & i \neq 5, \\ \begin{bmatrix} 0 & 1 & 0 \\ -1 & 0 & 0 \\ 0 & 0 & 0 \end{bmatrix} \dfrac{\left[\vec{u}^{x}_{D,i}\; \vec{u}^{y}_{D,i}\; 0\right]^T}{\|\left[\vec{u}^{x}_{D,i}\; \vec{u}^{y}_{D,i}\; 0\right]\|} & i = 5, \end{cases} \tag{13}$$

where the components of the drag direction vector are given by the dot product with the appropriate unit vector of the kite coordinate system, $\vec{u}^{(\cdot)}_{D,i} = \vec{u}_{D,i} \cdot (\cdot)_k$. Note that $i = 5$ refers to the vertical stabilizer, thus requiring the case structure of (13).

Using this methodology, the kite hydrodynamic model can capture the differences in flow velocities experienced by each of the hydrodynamic surfaces (wings, horizontal stabilizer, fuselage, and vertical stabilizer) caused by wave velocity contributions and turbulence. For the control-oriented kite model that we have developed, our hydrodynamic model serves as a reasonable approximation for the fluid dynamic forces that would be encountered, allowing simulations to be performed in tens of minutes, instead of the hours or days that would be required to simulate the model using a computational fluid dynamics (CFD) solver, so that control strategies can be rapidly developed.

B. Kite Tether and Mooring Line Model

The kite's tether and platform mooring lines are modeled as chains of non-compressive spring-dampers (links), connected with point masses (nodes), subjected to buoyancy, gravity, and drag. The subscript u is used to index to the mooring lines and kite tether, with $u = 1$ denoting the kite's tether and $u = 2, 3, 4$ denoting the platform's mooring lines. The subscript c is used to denote the individual lumped mass where $c = 1, 2, \ldots, N_c$, and N_c is the total number of lumped masses per mooring line or tether. The net force for each lumped mass in the mooring line and the kite's tether, $\vec{F}_{line,u_c}$, is calculated by:

$$\begin{aligned} \vec{F}_{line,u_c} = \frac{1}{2}\big((\rho - \rho_{T,u_c})\pi r_T^2 l_{T,u_c} g \vec{z}_o \\ + \frac{1}{2}\rho\|\vec{v}_{a,T,u_c}\|^2 A_{p,T,u_c} C_{D,T,u_c} \frac{\vec{v}_{a,T,u_c}}{\|\vec{v}_{a,T,u_c}\|} \\ + \vec{F}_{Ten,u_c}\big) \end{aligned}$$

$$\text{where} \quad u = 1, 2, 3, 4 \tag{14}$$

where ρ_{T,u_c} is the density of the tether or mooring line link, r_{T,u_c} is the radius of the tether or mooring line link, l_{T,u_c} is the un-spooled tether length or constant mooring line link length, A_{p,T,u_c} is the area of the tether or mooring line link projected in the direction of the apparent flow, C_{D,T,u_c} is the drag coefficient of the tether or mooring line link, and $\vec{v}_{a,T,u_c}$ is the apparent flow speed at the midpoint of the tether link or mooring line. Lastly, $\vec{F}_{Ten,u_c}$ is the nonlinear spring-damper force, which is equal to the zero vector if $\|\mathbf{r}_{\vec{\mathbf{u}}_\mathbf{c}}\| < l_{T,u_c}$. If $\|\mathbf{r}_{\vec{\mathbf{u}}_\mathbf{c}}\| \geq l_{T,u_c}$, $\vec{F}_{Ten,u_c}$, is calculated as:

$$\begin{aligned} \vec{F}_{Ten,u_c} = \frac{1}{2}\Bigg(- E_{y,u_c} \frac{\pi r^2_{T,u_c}}{l_{T,u_c}} \left(\|\mathbf{r}_{\vec{\mathbf{u}}_\mathbf{c}}\| - l_{T,u_c}\right) \\ - 2\zeta_u \sqrt{E_{y,u_c} \frac{\pi r^2_{T,u_c}}{l_{T,u_c}} m_{u_c}} \frac{d}{dt}\|\mathbf{r}_{\vec{\mathbf{u}}_\mathbf{c}}\| \Bigg) \frac{\mathbf{r}_{\vec{\mathbf{u}}_\mathbf{c}}}{\|\mathbf{r}_{\vec{\mathbf{u}}_\mathbf{c}}\|} \end{aligned} \tag{15}$$

where E_{y,u_c} is the Young's modulus of the tether or mooring line links, ζ_{u_c} is the non-dimensional damping ratio for the tether or mooring line links, m_{u_c} is the damping mass for the tether or mooring line links, and $\mathbf{r}_{\vec{\mathbf{u}}_\mathbf{c}}$, is the vector from the origin to the each lumped mass of the tether and mooring line.

The total force acting at the platform from the three mooring lines, and at the kite from the kite's tether, can then be calculated. These forces are given as $\vec{F}_{line,u}$ and act at a distance from the center of mass of the platform given by the vector $\vec{r}_{p_u/p}$ for the mooring lines, and at the kite's center of mass for the kite's tether, denoted by the point k.

C. Lumped Mass Floating Platform Model

The floating platform is modeled in six degrees of freedom and is described by three principal body-fixed unit vectors, $\vec{x}_p$, $\vec{y}_p$, and $\vec{z}_p$, whose origin lies at the platform's center of mass, denoted by the point p. The nonlinear equations of motion describing the platform are given by:

$$\dot{\vec{\mu_p}} = f(\vec{\mu_p}, \vec{\omega_p}) \tag{16}$$

$$\mathrm{J_p}\dot{\vec{\omega_p}} = \vec{M}_{Net,p} - \vec{\omega_p} \times \mathrm{J_p}\vec{\omega_p} \tag{17}$$

$$\dot{\vec{r}}_{p/o} = \mathrm{R}(\vec{\mu_p})\vec{v_p} \tag{18}$$

$$\mathrm{M_p}\dot{\vec{v_p}} = \left(\vec{F}_{Net,p} - \mathrm{M_p}\vec{\omega_p} \times \vec{v_p}\right) \tag{19}$$

where $\vec{\mu_p} \triangleq [\,\phi_p \quad \theta_p \quad \psi_p\,]^T$ represents the vector of roll (ϕ_p), pitch (θ_p), and yaw (ψ_p) Euler angles, $\mathrm{J_p} \in \mathbb{R}^{3\times3}$ is the inertia matrix, and $\vec{M}_{Net,p}$ is the sum of all applied moments, expressed in the body-frame. The position vector, $\vec{r}_{p/o} \in \mathbb{R}^3$, is the vector from the point o to the point p, expressed in the ground-frame. The vector $\vec{v_p}$ is the associated body-frame velocity, and the matrix $\mathrm{R} \in \mathbb{R}^{3\times3}$ is the rotation matrix from the body frame to the ground frame. The variable $\mathrm{M_p} \in \mathbb{R}^{3\times3}$ is the apparent mass matrix, $\vec{F}_{Net,p}$ is the sum of all forces applied to the kite expressed in the body-frame, and $\vec{\omega_p} \triangleq [\ \omega_{x,p} \quad \omega_{y,p} \quad \omega_{z,p}\ ]^T$ is the body-frame angular velocity of the kite. Finally, the function $\vec{f}(\vec{\mu_p}, \vec{\omega_p})$ describing the rotational rates about the platform's axes is given by:

$$\vec{f}(\vec{\mu_p}, \vec{\omega_p}) = \begin{bmatrix} p_p \\ q_p \\ r_p \end{bmatrix} \tag{20}$$

where

$$\begin{aligned} p_p = {} & \omega_{x,p} + \omega_{y,p} \sin(\phi_p) \tan(\theta_p) \\ & + \omega_{z,p} \cos(\phi_p) \tan(\theta_p), \end{aligned} \tag{21}$$

$$q_p = \omega_{x,p} \cos(\phi_p) - \omega_{z,p} \sin(\phi_p), \text{ and} \tag{22}$$

$$r_p = \big(\omega_{y,p} \sin(\phi_p) + \omega_{z,p} \cos(\phi_p)\big) \sec(\theta_p). \tag{23}$$

To calculate the forces acting on the platform, the platform is modeled as a collection of lumped masses, shown in Fig. 6, all at a constant distance, denoted by $\vec{r}_{m_n/p}$, from the platform's center of mass. This method is based on [23], although we subsequently describe an important adaptation that we have made to the method of [23] to avoid jump discontinuities in the dynamic model. Each lumped mass is denoted with the subscript n, where $n \in \{1, 2, \ldots, N_p - 1, N_p\}$ and N_p is the total number of lumped masses used to describe the platform. Each lumped mass experiences a portion of the wave forces acting on the platform (which include the inertial and drag forces) and the platform's total gravity and buoyancy forces.

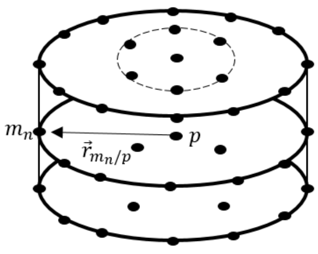

Fig. 6: The above figure shows a lumped mass representation of a cylindrical platform, not drawn to scale.

To smooth the jump discontinuities that would occur if a lumped *point* mass were to exit the water, each lumped mass element within the platform model is assigned a radius, r_m, where the forces acting on a partially submerged element are computed based on the fraction of that element's volume that is submerged, denoted by d_n. Specifically, for partially submerged elements, d_n multiplies the forces that *would be* acting on the lumped mass element *if* it were completely submerged. The value of d_n is calculated as follows for each lumped mass element:

$$d_n = \begin{cases} 0 & h_{z,n} - \vec{r}_{m_n/o}\vec{z}_o < -r_m \\ .5 + \frac{h_{z,n} - \vec{r}_{m_n/o}\vec{z}_o}{2r_m} & -r_m < h_{z,n} - \vec{r}_{m_n/o}\vec{z}_o < r_m \\ 1 & h_{z,n} - \vec{r}_{m_n/o}\vec{z}_o > r_m, \end{cases} \tag{24}$$

where $h_{z,n}$ is the height of the ocean at each lumped mass's position. The buoyant force for each lumped mass, $\vec{f}_{b,n}$, is calculated as:

$$\vec{f}_{b,n} = \rho \frac{V_p}{N_p} g \tag{25}$$

where V_p is the is the total volume of the platform. The gravitational force for each lumped mass, $\vec{f}_{g,n}$, is calculated as:

$$\vec{f}_{g,n} = \rho \frac{m_p}{N_p} g \tag{26}$$

where m_p is the total mass of the platform.

The forces due to the ocean current and waves are calculated using Morison's equation, [24] where the hydrodynamic force is a combination of the inertial and drag forces. Morison's wave force approximation is valid in regions where the ratio of the wave height to the diameter of the platform is small or the ratio of the wave height to the diameter of the platform is large [24]. For a small platform, (such as the one used in this work), this is a reasonable assumption for both small wave heights (such as the heights typically experienced at the location studied) and extreme wave heights. This force is computed at each lumped mass, assuming that each lumped mass on the surface of the platform contains a portion of the surface area of the platform, denoted as A_n. For each lumped mass, the hydrodynamic forces, $f_{f,n}$, are computed by:

$$f_{f,n} = \begin{cases} 0 & n \in n_i \\ f_{mor} & n \in n_o \end{cases} \tag{27}$$

where n_i and n_o are the set of lumped masses on the interior and surface of the platform respectively, and:

$$f_{mor} = \rho \frac{V_p}{N_p} \dot{v}_f + \rho C_a \frac{V_p}{N_p} \dot{\vec{v}}_{rel,n} + \frac{1}{2} \rho C_d A_n \vec{v}_{rel,n} |\vec{v}_{rel,n}|, \tag{28}$$

$$\vec{v}_{rel,n} = \vec{v}_f - (\dot{\vec{r}}_{p/o} + \vec{\omega_p} \times \vec{r}_{m_n/p}), \tag{29}$$

$$\dot{\vec{v}}_{rel,n} = \dot{v}_f - (\vec{\alpha_p} \times \vec{r}_{m_n/p} + \ddot{\vec{r}}_{p/o} + \vec{\omega_p} \times \vec{\omega_p} \times \vec{r}_{m_n/p}), \tag{30}$$

where f_{mor} is the force from Morison's equation, $\vec{v}_{rel,n}$ is the relative velocity at each lumped mass, C_a is an added mass coefficient for each surface lumped mass, calculated based on the platform surface geometry, and C_d is a drag coefficient for each surface lumped mass calculated based on the Keulegan–Carpenter number.

From equations (15), (25), (26), and (27), the total force acting on the platform can be computed by the equation:

$$\vec{F}_{Net,p} = \sum_{n=1}^{N_p} \left(\vec{f}_{b,n} + \vec{f}_{g,n} + \vec{f}_{f,n} \right) + \sum_{u=1}^{4} \vec{F}_{line,u}. \tag{31}$$

Similarly, the moments acting on the platform can be calculated by:

$$\vec{M}_{Net,p} = \sum_{n=1}^{N_p} \vec{r}_{m_n/p} \times \left(\vec{f}_{b,n} + \vec{f}_{g,n} + \vec{f}_{f,n}\right) + \sum_{u=1}^{4} \vec{r}_{p_u/p} \times \vec{F}_{line,u}. \tag{32}$$

III. OCEAN MODELING

In this work, three different flow characterizations have been used to test the kite and floating platform system. They are:

- *Constant flow environment:* A constant flow field, $\tilde{V}_{const}$, aligned with the ground-frame $\vec{x}_o$ direction.
- *Non-turbulent flow environment with wave effects:* A constant flow field aligned with the ground-frame $\vec{x}_o$ direction with superimposed planar progressive waves that vary with $\vec{x}_o$, $\vec{z}_o$, and time. Here, the total flow velocity is given by $\tilde{V}_{const} + \tilde{V}_{wave}(\vec{x}_o, \vec{z}_o, t)$.
- *Turbulent flow environment with wave effects:* A data-driven flow field taken from the both observed and modeled ocean current data with superimposed turbulence varying with $\vec{y}_o$, $\vec{z}_o$, and time, and superimposed planar progressive waves varying with $\vec{x}_o$, $\vec{z}_o$, and time. Here, the total flow velocity is given by $\tilde{V}_{comb}(\vec{y}_o, \vec{z}_o, t) + \tilde{V}_{wave}(\vec{x}_o, \vec{z}_o, t)$.

A. Spatiotemporally Constant Flow Field

The constant flow field, $\tilde{V}_{const}$, can be described by the equation:

$$\tilde{V}_{const} = \begin{bmatrix} V_x \\ 0 \\ 0 \end{bmatrix} \tag{33}$$

where V_x is a prescribed constant flow speed in m/s. The simulation results in this paper focus on the western portion of the Gulf Stream, adjacent to Cape Hatteras, as a candidate site, and flow speeds are selected accordingly.

B. Wave Modeling

In this work, the waves are modeled as planar progressive waves, as shown in [24], and are assumed to be deep-water waves. This assumption is valid when the kite to be deployed in locations where the depth is greater than half the wavelength of the waves, which applies to all of the candidate sites being considered. From this formulation, the free surface elevation of the wave, η, is given by:

$$\eta = A_w \cos(KR_x - \omega_w t + \epsilon_w) \tag{34}$$

where A_w is the wave amplitude, K is the wavenumber, ω_w is the wave frequency, R_x is the component of any generic position vector aligned with the ground-frame $\vec{x}_o$ direction, and ϵ_w is the phase offset. This equation, with the addition of the vertical offset of the unperturbed sea surface as measured from the ocean floor, allows for the $\vec{z}_o$ coordinate of the ocean surface, denoted as h_z in equation (24), to be calculated for each platform lumped mass. The horizontal and vertical velocities, u_{wave} and w_{wave} respectively, can then be calculated as:

$$u_{wave} = \omega_w A_w e^{K(\eta - R_z)} \cos(KR_x - \omega_w t), \tag{35}$$

$$w_{wave} = \omega_w A_w e^{K(\eta - R_z)} \sin(KR_x - \omega_w t) \tag{36}$$

where the generic R_z is the depth component of any position vector expressed in the ground frame. For deep water waves, the wavenumber is calculated as:

$$K = \frac{\omega_w^2}{g}. \tag{37}$$

These flow components are then placed in a vector to form $\tilde{V}_{wave}$, as follows:

$$\tilde{V}_{wave} = \begin{bmatrix} u_{wave} \\ 0 \\ w_{wave} \end{bmatrix}. \tag{38}$$

C. Realistic Spatiotemporally Varying Flow Field Implementation

The flow field, which is characterized as a function of depth ($\vec{z}_o$), cross-current location ($\vec{y}_o$), and time (t), is computed as the superposition of a low-frequency flow profile and high-frequency turbulence model, as:

$$\tilde{V}_{comb}(\vec{y}_o, \vec{z}_o, t) = \tilde{V}_{turb}(\vec{y}_o, \vec{z}_o, t) + \tilde{V}(\vec{z}_o, t) \tag{39}$$

where $\tilde{V}(\vec{y}_o, \vec{z}_o, t)$, $\tilde{V}_{turb}(\vec{y}_o, \vec{z}_o, t)$, and $\tilde{V}_{comb}(\vec{y}_o, \vec{z}_o, t)$ represent the low-frequency flow field, high-frequency turbulent field, and combined flow model, respectively. Because the total cross-current motion of the kite spans a tiny fraction of the total current resource (e.g., the Gulf Stream), spatial variations in $\vec{y}_o$ are neglected in the low-frequency model.

1) Low-Frequency Ocean Modeling: The kite dynamic model has been designed to accept any low-frequency ocean data or model outputs, provided that they are indexed both by depth and time. For the simulation studies presented in this work, the Mid-Atlantic Bight, South Atlantic Bight Regional Ocean Model (MSR) was used as the primary source of low-frequency ocean flow information. This model, which was developed by North Carolina State University's Ocean Observing and Modeling Group, provides current profiles at 42 different locations in the Gulf Stream at 25 m vertical resolution. Each data set provides flow velocity vectors, $\tilde{V}(\vec{z}_o, t)$, along the water column (i.e., the $\vec{z}_o$ direction). The MSR model is detailed in [31].

2) Modeled High-Frequency Turbulent Variability: The turbulent high-frequency components of the ocean currents are calculated based on a discretization of the flow velocity's power spectral density (PSD) equation. Specifically, the model leverages fundamental techniques described in [18] to generate a spatiotemporally varying turbulence profile that can be applied to the hydrodynamic center of each component in the dynamic model. Based on inputs of turbulence intensity, time-averaged flow velocity profile, a specified frequency range, standard deviations and spatial correlation coefficients for the flow velocities, the model outputs a spatial grid of time-varying velocity vectors on the inlet plane (which is n_y by n_z, having indices i and j ranging from 1 to n_y and 1 to n_z). The continuous PSD of flow velocity, $G(f)$, where f represents frequency, is given as:

$$G(f) \propto f^{-\frac{5}{3}} \tag{40}$$

which implies G^m, the one-sided PSD, is equal to:

$$G^m(f) = A_m f^{-\frac{5}{3}}. \tag{41}$$

Here, A_m is a constant defined by the equation:

$$A_m = \frac{2\overline{U}^2 T_m^2}{3\left[\frac{1}{f_{min}^{\frac{2}{3}}} - \frac{1}{f_{max}^{\frac{2}{3}}}\right]} \tag{42}$$

where m is an index to the u, v, or w velocity components, f_{min} and f_{max} define the frequency range of the turbulence, $\overline{U}$ is the magnitude of the time-averaged flow velocities, $\overline{u}$, $\overline{v}$, and $\overline{w}$, defined as:

$$\overline{U} = \sqrt{\overline{u}^2 + \overline{v}^2 + \overline{w}^2} \tag{43}$$

and where turbulence intensity, denoted by T_m, is equal to:

$$T_m = \frac{\sigma_m}{\overline{U}} \tag{44}$$

where the standard deviations (σ_m) in the downstream, cross-current, and down directions are calculated as:

$$\sigma_u = \frac{T_u}{\sqrt{1 + P^2 + Q^2}}, \sigma_v = P\sigma_u, \text{ and } \sigma_w = Q\sigma_u. \tag{45}$$

Here, P and Q are constants that relate the standard deviations in the cross-current and down directions to the standard deviation in the the downstream direction.

Correlated velocity components are then generated by a discretized one-sided PSD equation, $\tilde{s}^m(\vec{f}) = G^m(f)\delta f$, where $\vec{f}$ is the vector of user-selected frequencies, chosen to capture the characteristic frequencies of the flow field, $\vec{f} \triangleq f_1, f_2.....f_n$. A coherence function, C_{ij}, defining the flow component's correlation between any two grid nodes on the inlet plane, is defined by:

$$C_{ij}(\vec{f}) = \exp\left(-\frac{R_c \Delta r_{ij} \vec{f}}{\overline{U}}\right) \tag{46}$$

where Δr_{ij} is the distance between any two inlet plane grid nodes and R_c is a coherence decay constant. The amplitude of the fluctuating velocity component, S^m, is written as:

$$S_{ij}^m(\vec{f}) = 2C_{ij}(\vec{f}) A_m \vec{(f)}^{-\frac{5}{3}} \delta f. \tag{47}$$

The velocity weighting factor, $H(\vec{f})$, is then calculated in frequency domain as:

$$\begin{aligned}
&H_{11}^m(\vec{f}) = S_{11}^m(\vec{f})^{\frac{1}{2}}, H_{21}^m(\vec{f}) = \frac{S_{21}^m(\vec{f})}{H_{11}^m(\vec{f})},\\
&H_{22}^m(\vec{f}) = (S_{22}^m(\vec{f}) - H_{21}^m(\vec{f})^2)^{\frac{1}{2}}, H_{31}^m(\vec{f}) = \frac{S_{31}^m(\vec{f})}{H_{11}^m(\vec{f})},\\
&H_{ij}^m(\vec{f}) = \frac{(S_{ij}^m(\vec{f}) - \sum_{l=1}^{l=j-1} H_{il}^m(\vec{f}) H_{jl}^m(\vec{f}))}{H_{jj}^m(\vec{f})},\\
&H_{jj}^m(\vec{f}) = (S_{jj}^m(\vec{f}) - \sum_{l=1}^{l=j-1} H_{jl}^m(\vec{f})^2)^{\frac{1}{2}},
\end{aligned} \tag{48}$$

where H_{ij}^m is the element in the i^{th} row and the j^{th} column of $H \in \mathbb{R}^{n_y n_z \times n_y n_z}$. The velocity weighting factor, $H_{ij}^m(\vec{f})$, is then used to calculate analytical expressions for the velocity components, u, v, and w, as functions of time. The amplitude of the fluctuating velocity component, m_{kj}^*, can be represented as:

$$m_{kj}^* = \sum_{l=1}^{j} H_{lj}^m(f_k) e^{i\theta_{kl}} \tag{49}$$

where θ_{kl} is a random phase angle between 0 and 2π. Because $m_{kj}^* = |m_{kj}^*| e^{i\theta_{kj}}$, where θ_{kj} is the resultant phase angle associated with each frequency component at each grid point, j, m_{kj}^* can be converted from frequency domain to time domain, where each fluctuating velocity component is denoted as:

$$m_j(t) = \sum_{k=1}^{N} |m_{kj}^*| \sin(2\pi f_k^* t + \theta_{kj}). \tag{50}$$

This calculation results in a grid of velocity vectors at each node of the inlet plane.

IV. CONTROL FORMULATION

The control system is designed to achieve two objectives: (i) Traverse a prescribed cross-current path that results in high tether tensions and (ii) strategically switch between spool-out and spool-in behavior in a manner that keeps the kite in a relatively consistent depth and flow range. The former is accomplished via a hierarchical controller, whereas the latter is accomplished through an intra-cycle spooling controller. The complete control system block diagram is shown in Fig. 7.

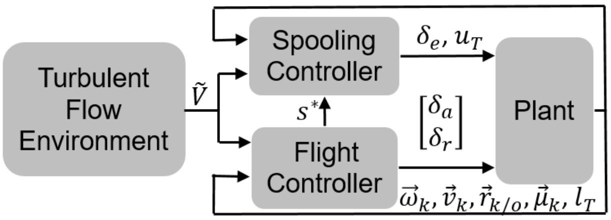

Fig. 7: Block diagram showing the controller's interaction with the plant and environment, where l_T is the un-spooled tether length.

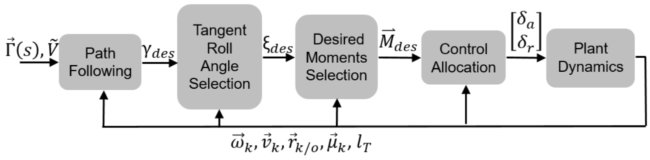

Fig. 8: Block diagram showing the flight controller from Fig. 7.

A. Flight Controller

The flight controller, which enables the kite to track a prescribed figure-8 path, contains four levels. This modular, hierarchical control structure is motivated by prior work in [32] and is partitioned into:

1) A *path-following controller* that accepts the path geometry and outputs a desired velocity angle as defined in [33].
2) A *tangent roll angle controller*, which accepts a desired velocity angle, $\gamma(\vec{v}_{des})$, and outputs a desired tangent roll angle, ξ_{des}, which is the angle between $\vec{y}_k$ and the plane tangent to the surface of the sphere of radius $\|\vec{r}_{k/p}\|$ at the kite's position, termed the *tangent plane* (shown in Fig. 1) – this angle dictates the component of hydrodynamic lift that contributes to turning.
3) A *desired moment controller*, which accepts the tangent roll setpoint and side-slip angle setpoint, and outputs a desired moment vector.
4) A *control allocation module*, which accepts the desired moment vector and computes the required control surface deflections for the ailerons, elevator, and rudder.

A block diagram of this controller can be seen in Fig. 8.

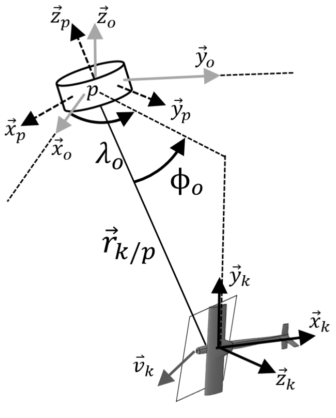

Fig. 9: The above figure shows the spherical coordinates λ_o and Φ_o and the vector from the platform to the kite, $\vec{r}_{k/p}$.

1) Path Following Controller: The target cross-current path, $\vec{\Gamma}(s)$, is specified in Cartesian coordinates based on the Lemniscate of Booth, defined by a_{booth} and b_{booth} in [32]. This path is constrained to lie on the surface of a sphere centered at the center of mass, p, of the floating platform, as shown in Fig. 9. The variable s is a path parameter that varies from 0 to 2π. Given this path, the controller calculates a three-dimensional vector representing the desired direction of the kite's velocity vector, which is computed as a weighted average between the *perpendicular vector*, $\vec{p}_{\perp}^{\,*}$, and the *parallel vector*, $\vec{p}_{\|}^{\,*}$. The perpendicular vector is given by:

$$\vec{p}_{\perp}^{\,*} = \frac{\hat{p}_{\perp}}{\|\hat{p}_{\perp}\|} \quad \text{where} \quad \hat{p}_{\perp} = \begin{bmatrix} (\vec{\Gamma}(s^*) - \vec{x}) \cdot \vec{u}_{\Phi_o}(\vec{x}) \\ (\vec{\Gamma}(s^*) - \vec{x}) \cdot \vec{u}_{\lambda_o}(\vec{x}) \\ 0 \end{bmatrix}. \tag{51}$$

Here, $\vec{u}_{\Phi_o}(\vec{x})$ and $\vec{u}_{\lambda_o}(\vec{x})$ are unit vectors in the elevation (Φ_o) and azimuth (λ_o) directions shown in Fig. 1, sometimes referred to as "local north" and "local east." The parallel vector, $\vec{p}_{\|}^{\,*}$, is a unit vector that lies parallel to the path at the path variable corresponding to the closest point on the path, s^*, and is calculated by:

$$\vec{p}_{\|}^{\,*} = \frac{\hat{p}_{\|}}{\|\hat{p}_{\|}\|} \quad \text{where} \quad \hat{p}_{\|} = \left.\frac{d\vec{\Gamma}}{ds}\right|_{s=s^*}. \tag{52}$$

In (51) and (52), the closest point on the path is described by the path variable s^*, which is the solution to the minimization problem:

$$\begin{aligned} s^* &= \arg\min_s \ \alpha(s), \quad \text{where} \\ \tan\left(\alpha(s)\right) &= \frac{\|\vec{r}_{k/p} \times \vec{\Gamma}(s)\|}{\vec{r}_{k/p} \cdot \vec{\Gamma}(s)}. \end{aligned} \tag{53}$$

Here, $\alpha(s)$ is the angle between the position vector, $\vec{r}_{k/p}$, and the path, $\vec{\Gamma}(s)$.

The desired velocity unit vector, $\vec{v}_{des}$, is then calculated as the linearly weighted sum of $\vec{p}_{\perp}^{\,*}$ and $\vec{p}_{\|}^{\,*}$, according to:

$$\begin{aligned} \overline{\alpha}(s^*) &= \min\left\{\alpha(s^*), \alpha_0\right\} \\ \vec{v}_{des} &= \left(1 - \frac{\overline{\alpha}(s^*)}{\alpha_0}\right)\vec{p}_{\|}^{\,*} + \frac{\overline{\alpha}(s^*)}{\alpha_0}\vec{p}_{\perp}^{\,*}. \end{aligned} \tag{54}$$

Here, α_0 serves as an upper limit on the angle used in the weighting.

The velocity angle, γ, which describes the orientation of a given velocity vector on the sphere of radius $\|\vec{r}_{k/p}\|$ at the current position $\vec{r}_{k/p}$, is given by:

$$\gamma(\vec{v_k}) = \arctan\left(\frac{\vec{v_k} \cdot \vec{u}_{\Phi_o}(\vec{r}_{k/p})}{\vec{v_k} \cdot \vec{u}_{\lambda_o}(\vec{r}_{k/p})}\right). \tag{55}$$

The desired velocity angle is therefore given by $\gamma(\vec{v}_{des})$.

2) Tangent Roll Angle Controller: The next level of the flight controller maps $\gamma(\vec{v}_{des})$ to a desired tangent roll angle, ξ_{des}, where ξ describes the kite's orientation relative to the tangent plane and is calculated as:

$$\tan\left(\xi(\vec{y}_k(t))\right) = \frac{\vec{y}_k \cdot (\vec{u}_{\lambda_o} \times \vec{u}_{\Phi_o})}{\sqrt{(\vec{y}_k \cdot \vec{u}_{\Phi_o})^2 + (\vec{y}_k \cdot \vec{u}_{\lambda_o})^2}}. \tag{56}$$

The desired tangent roll angle, ξ_{des}, is calculated using saturated proportional control, specifically:

$$\xi_{des} = \min\{\max\{k_\gamma\left(\gamma(\vec{v}) - \gamma(\vec{v}_{des})\right), \xi_{min}\}, \xi_{max}\} \tag{57}$$

where k_γ is the proportional gain. Ultimately, adjustment of ξ re-vectors the kite's lift to provide the necessary force to re-align the kite's velocity angle with the target value and ultimately get the kite back on its target path.

3) Desired Moment Vector Controller: In selecting the desired moments, we set a target rolling moment to drive the tangent roll angle (ξ) to its setpoint (ξ_{des}), whereas we set a target yaw moment to drive the side-slip angle, β, to zero. The tether spooling controller articulates the elevator to trim the system to a high angle of attack during spool-out and a low angle of attack during spool-in (which is described in the subsequent sub-section). The desired moment vector set within the flight controller is given by:

$$\vec{M}_{des} = \begin{bmatrix} k_{p_L} e_\xi(t) + k_{i_L} \int_0^t e_\xi(t) d\tau + k_{d_L} \dot{e}_\xi(t) \\ 0 \\ k_{p_N} \beta + k_{i_N} \int_0^t \beta d\tau + k_{d_N} \dot{\beta} \end{bmatrix}$$

where $e_\xi(t) = \xi(\vec{y}_k(t)) - \xi_{des}$, and β is the fluid dynamic side-slip angle.

4) Control Allocation Module: In order to map the desired moment vector to control surface deflections, we invert a linearized approximation of the nonlinear mapping from deflections to hydrodynamic moments. This approximation is calculated by neglecting the effect of angular velocity on the apparent flow at each fluid dynamic surface, then linearizing to obtain an expression in the following form:

$$\vec{M}_{Net,p} = \vec{M}_o + A\vec{\delta} \tag{58}$$

where $\vec{\delta} \triangleq [\ \delta_a\ \delta_e\ \delta_r\,]^T$ represents the deflection angles of the ailerons, elevator, and rudder, respectively. The variable $\vec{M}_o$ represents the moment vector that occurs with zero control surface deflections, and A is the matrix of linear control sensitivity coefficients. This results in a system of three equations and three unknowns, which are solved in computing the control surface deflections at each time instant.

B. Winch (Spooling) Controller

The commanded rate of tether release, $u_T(t)$, is set by a spooling controller that seeks to spool tether out while the kite is flying at a high angle of attack during the portions of the lap in which large tensions are possible, then spool tether in while the kite is at a low angle of attack during the remainder of the lap. The intra-cycle spooling algorithm in this work is designed to maintain a consistent tether length each lap, represented by the constraint:

$$\int_{t_{0,j}}^{t_{f,j}} \tilde{u}_j(\tau) d\tau = 0. \tag{59}$$

where the index j refers to the lap number. This ensures that the kite remains at a consistent depth within the ocean shear profile. In attempting to find the command sequence that satisfies this constraint, we make two key simplifying assumptions:

- The winch is capable of achieving the commanded speed quickly, relative to the rate of change of the command.
- The commanded spooling speed is piecewise constant over each of N_R "spooling regions", and alternates between spooling in and spooling out at a prescribed speed, u_{spool}.

The first approximation will hold for a well-designed winch/generator system, meaning that $\tilde{u}_T(t) \approx u_T(t)$. The two approximations together mean that the constraint equation of (59) can be written as:

$$0 = \mathbf{1}^{1 \times N_R} \underline{U}^{j-1} \Delta_T^j \tag{60}$$

where the matrix $\underline{U}^{j-1} \in \mathbb{R}^{N_R \times N_R}$ is a diagonal matrix where the element in the p^{th} and q^{th} column is given by:

$$\underline{U}_{p,q}^{j-1} = \begin{cases} u_{spool}^{j-1} & p = q = \text{odd} \\ -u_{spool}^{j-1} p = q = \text{even} \\ 0 & p \neq q. \end{cases} \tag{61}$$

Here, u_{spool}^{j-1} is one third of the mean flow speed at the vehicle CM over the last lap of the system. This is proven to be the optimal spool-out speed through a quasi-steady analysis performed by [8]. The vector $\Delta_T^j \in \mathbb{R}^{N_R}$ contains the time durations required to traverse a specific section of the path during the next (j^{th}) lap. Because the timings of the next lap are not known beforehand, it is desirable to define our tether spooling controller in terms of the path variable, s, *not* time. Therefore, we transform the time-domain constraint of (60) to a path-domain constraint using a numerical approximation of the time derivative of the path variable from the previous lap in each spooling region. Here, we denote the spooling region with the index $i_R = 1, 2, \ldots, N_R$. Specifically, we approximate the i_R^{th} element of Δ_T^j, written as Δ_{T,i_R}^j, in terms of the path variable using logged data from the previous lap, $j-1$. Specifically,

$$\Delta_{T,i_R}^j \approx \frac{s_{i_R+1}^{j-1} - s_{i_R}^{j-1}}{\delta s_{i_R}^{j-1}} \tag{62}$$

$$= \begin{bmatrix} \frac{1}{\delta s_1^{j-1}} & 0 & \cdots & 0 \\ 0 & \frac{1}{\delta s_2^{j-1}} & \cdots & 0 \\ \vdots & \vdots & \ddots & \vdots \\ 0 & 0 & 0 & \frac{1}{\delta s_{N_R+1}^{j-1}} \end{bmatrix} \underline{D} \begin{bmatrix} s_1^{j-1} \\ s_2^{j-1} \\ \vdots \\ s_{N_R+1}^{j-1} \end{bmatrix} \tag{63}$$

$$\triangleq \underline{\delta s}^j \underline{D} S^{j-1}. \tag{64}$$

Note that $s_{i_R}^{j-1}$ refers to the value of the path variable at the end of the i_R^{th} region during the previous lap, $j-1$. Additionally, $\delta s_{i_r}^{j-1}$ is the mean of the derivative of $s(t)$ over the i_R^{th} section of the path. Furthermore, because the path is defined using a path variable $s \in \{0, 1\}$, $s_{N_R+1}^j = 1$ for all j. The discrete difference operation matrix, $\underline{D} \in \mathbb{R}^{N_R \times N_R}$, is a matrix with ones along the main diagonal and negative ones on the diagonal underneath the main diagonal. Thus, after every lap, the problem of meeting our approximation of the net-zero spooling constraint becomes one of solving an approximated version of the constraint equation:

$$0 = \mathbf{1}^{1 \times N_R} \underline{U}^{j-1} \underline{\delta s}^{j-1} \underline{D} S^j \tag{65}$$

for the vector $S^j \in \mathbb{R}^{N_R+1}$, the elements of which define the spooling regions for the next lap. Note that in general, this is a single scalar equation and cannot be solved uniquely for the elements of S^j. However, if we prescribe a structure to the spooling regions, we can reduce the number of parameters that define the spooling regions to one, resulting in a unique solution. In the case of the figure-8 path geometry, we know that the tension profile over the course of a figure-8 exhibits two local minima, which occur roughly at $s = 0.25$ and $s = 0.75$. Therefore, our vector S^j takes the form:

$$S^j = \begin{bmatrix} 0.25 \\ 0.25 \\ 0.75 \\ 0.75 \\ 1 \end{bmatrix} + \begin{bmatrix} -1 \\ 1 \\ -1 \\ 1 \\ 0 \end{bmatrix} s^j_w. \qquad (66)$$

By substituting this expression into (65), we can solve directly for s^j_w, which defines the width of the spooling region for the next lap. This then defines a simple, switched spooling control structure:

$$\mathbf{u}^j_T(s^*(t)) = \begin{cases} u_{in} & 0.25 - s^j_w \leq s^*(t) \leq 0.25 + s^j_w \text{ or} \\ & 0.75 - s^j_w \leq s^*(t) \leq 0.75 + s^j_w, \\ u_{out} & \text{otherwise.} \end{cases} \qquad (67)$$

While (67) will yield zero net spooling under *nominal* conditions, it is not robust to disturbances that cause the actual flight speed (and therefore the time required to traverse a particular section of the figure-8) to differ from that which was used in computing $\mathbf{u}^j_T(s^*(t))$. To add robustness to the spooling strategy, we utilize a simple feedback controller to track a target tether length, $l^j_{T,SP}(s(t))$, which is obtained by integrating (67) over the path as follows:

$$l^j_{T,SP}(s(t)) = l_{T,0} + \int_0^{s(t)} \frac{\mathbf{u}^j_T(\sigma)}{\delta s^{j-1}} d\sigma. \qquad (68)$$

V. RESULTS

This section provides an extensive set of simulation results, evaluating quality of flight and energy production under three different flow field models and two different floating platform sizes. The parameters describing the kite, tether, platform, and mooring lines are given in Table I, and the parameters describing the kite controller are given in Table II.

All three of the flow models described in Section 3 were considered. As a reminder, these flow models included:

1) *Constant flow*, where the flow velocity vector was set to $\tilde{V}_{const}$ at all spatial locations and times;
2) *Non-turbulent flow with wave effects*, where the flow velocity vector was given by $\tilde{V}_{const} + \tilde{V}_{wave}(\vec{x}_o, \vec{z}_o, t)$; and
3) *Turbulent flow with wave effects*, where the flow velocity vector was given by $\tilde{V}_{comb}(\vec{y}_o, \vec{z}_o, t) + \tilde{V}_{wave}(\vec{x}_o, \vec{z}_o, t)$.

Results from the constant flow environment provided a benchmark lap-averaged power and peak-to-average power against which the performance under the other flow environments could be compared. By considering wave effects first in isolation (without the influence of underlying turbulence in the flow), then in combination with turbulence, the individual contributions of the waves and turbulence could be better understood.

TABLE I
KITE AND SMALL PLATFORM PARAMETERS

Variable	Description	Value	Units
M_k	Kite's mass	2857	kg
ρ	Density	1000	kg/m^3
$-$	Fuselage length	7.5	m
A_r	Reference area	10	m^2
$-$	Port wing chord	1	m
$-$	Port wing span	5	m
$-$	Starboard wing chord	1	m
$-$	Starboard wing span	5	m
$-$	Horizontal stabilizer chord	0.5	m
$-$	Horizontal stabilizer span	4.0	m
$-$	Vertical stabilizer chord	0.65	m
$-$	Vertical stabilizer span	2.438	m
$r_{T,1}$	Tether radius	7.2	mm
$-$	Average tether length	125	m
$E_{y,1}$	Tether youngs modulus	50	GPa
ζ_1	Tether damping ratio	0.75	$-$
m_1	Tether damping mass	2857	kg
$C_{D,T,1}$	Tether drag coefficient	0.5	$-$
$\rho_{T,1}$	Tether density	1300	kg/m^3
$r_{T,2-4}$	Mooring line radius	0.025	m
$E_{y,2-4}$	Mooring line Young's modulus	500	GPa
ζ_{2-4}	Mooring line damping ratio	0.3	$-$
m_{2-4}	Mooring line damping mass	226	Mg
$C_{D,T,2-4}$	Mooring line drag coefficient	0.5	$-$
$\rho_{T,2-4}$	Mooring line density	1300	kg/m^3
$-$	Platform diameter	12	m
$-$	Platform height	4	m
V_p	Platform volume	452	m^3

TABLE II
KITE CONTROLLER PARAMETERS

Variable	Description	Value	Units
α_0	Angle weighting limit	6	deg
k_γ	Tangent roll proportional gain	0.2	$-$
ξ_{min}	Min prescribed tangent roll	-20	deg
ξ_{max}	Min prescribed tangent roll	20	deg
k_{pL}	Roll moment proportional gain	630	kNm/rad
k_{iL}	Roll moment integral gain	0	Nm/rad s
k_{dL}	Roll moment derivative gain	630	kNms/rad
τ_L	Roll moment filter time const.	0.001	s
k_{pN}	Yaw moment proportional gain	0	Nm/rad
k_{iN}	Yaw moment integral gain	0	Nm/rad s
k_{dN}	Yaw moment derivative gain	0	Nm s/rad
τ_N	Yaw moment filter time const.	1	s
$-$	Path azimuth sweep	131.8	deg
$-$	Path elevation sweep	18.34	deg

In addition to considering the aforementioned three flow environments, two platform sizes were considered: a 4-meter high, small platform, and a fixed (effectively infinitely sized, so as to remain substantially stationary) platform. The smaller platform size was intended to reflect the sizing characteristics of a floating research station, whereas the infinitely large platform was chosen to emulate the sizing of an oil rig or platform of similar size.

The full suite of simulations considered is summarized in Table III.

TABLE III
SIMULATION SETS

Infinite Size Platform	**4 m Platform**
Constant Flow: Vx = 1 m/s	Non-Turbulent Flow with Waves: Vx = 1 m/s
Non-Turbulent Flow with Waves: Vx = 2 m/s	Turbulent Flow with Waves: Vx = 2 m/s
Turbulent Flow with Waves: Mean flow speed of 1.57 m/s	

A. Numerical Simulation

The complete system (kite, tethers, platform, controller, and environment) was simulated using the MathWorks product Simulink. The solver used in this work was Matlab's ODE23tb solver using a variable time step. For more information about this solver, please see MathWork's Matlab and Simulink documentation [34]. This solver was selected due to its ability to handle stiff numerical simulations efficiently. The stiffness in the simulation came from having time constants in the system that differ by an order of magnitude. The floating platform was simulated using 82 platform lumped masses and three anchor tethers each having two lumped masses. The kite's tether was simulated with two lumped masses. Additionally, the maximum time step used by the solver was 0.1 seconds.

B. Wave Parameter Selection

Two different approaches were taken when selecting wave parameters for the simulations. Under both approaches, the wave amplitude (or significant wave height), A_w, and wave period, T_w served as independent variables, which were linked to the critical parameters in the wave modeling framework of Section III-B through the following relationships:

$$A_w = H_s, \omega_w = \frac{2\pi}{T_p}, K = \frac{\omega_w^2}{g}, \text{and } \epsilon_w = 0. \tag{69}$$

In the first approach, observed data from the Coastal Data Information Program (CDIP) 192 Oregon Inlet Buoy, was used in order to identify and simulate the performance of the kite in the most commonly occurring wave periods (T_w) and wave heights (A_w). A two-dimensional wave data histogram for the Oregon Inlet Buoy was created, and is shown in Fig. 10, where peak period, T_p, (defined as the wave period with the highest energy) was binned by 1.5 second intervals and where significant wave height, H_s, (defined as the average wave height of the highest 1/3 of waves) was binned by 0.5 meter intervals. From this 2-D histogram, two wave parameter sets were created. By first looking down the significant wave height axis and then selecting the most commonly occurring significant wave height bins, the most commonly occurring significant wave heights in those bins were selected (for example, a significant wave height of 0.44 meters was the most common within the 0.0-0.5 meter bin). For each wave height bin, the most commonly occurring peak period was then selected. The results of this can be seen in Table IV. This same process was repeated by looking down the peak period axis and selecting the most commonly occurring peak period bins. From these bins, the most commonly occurring peak periods were selected (for example, a peak period of 2.76 seconds was the most common within the first bin). For each peak period bin selected, the most commonly occurring significant wave height was then selected. The results of this can be seen in Table V. Additionally, the $*$ symbol in each table indicates which wave parameter (H_s or T_p) was selected for study from the histogram in Fig. 10.

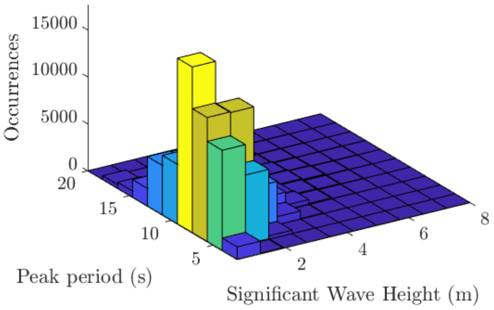

Fig. 10: The above histogram depicts the significant wave height and peak period versus occurrences taken from data over a span of approximately eight years (April 2012 to February 2020) from the CDIP 192 Oregon Inlet Buoy.

TABLE IV
MOST COMMONLY OCCURRING WAVE HEIGHTS PER BIN AND THE CORRESPONDING MOST COMMON PEAK PERIODS WITHIN THOSE BINS.

$T_p(s)$	$H_s(m)*$
9.26	0.44
8.05	0.78
7.98	1.21
8.41	1.71
8.64	2.22
9.45	2.72
10.2	3.21
10.9	3.72

The second approach focused on understanding the range of wave heights and periods over which a degradation in performance was observed. This was done by gridding the space of T_w and A_w corresponding to more substantial waves (especially in terms of wave height) and performing a comprehensive simulation analysis over the full grid. The grid of wave parameters was created by selecting common conditions and extreme conditions in both peak period and significant wave height from the Wave Information Studies Hindcast model [26] and gridding the space in between. The extreme conditions examined, observed from [26], consisted of wave heights up to 16 meters with periods up to 20 seconds. Different grid limits and levels of discretization were used for the different flow cases with waves specified in Table III, owing to the fact that the kite experienced degradation in performance under different wave parameter (period and amplitude) thresholds, depending on the mean flow and the floating platform size present for each case.

By identifying the most commonly occurring wave periods and heights (along with the probability density associated with any given wave period and height) from the Oregon Inlet data *and* identifying the ranges of period and height over which performance degradation was seen, it was possible to quantify the robustness of the kite and its corresponding control algorithm.

C. Oregon Inlet Waves: Results

Results of simulating the kite's closed-loop performance under the commonly-occurring wave conditions identified based on the Oregon Inlet Buoy are summarized in Figs. 11, 12, 13, and 14. Additionally, a visualization of the kite's figure-8 path can be seen in Fig. 15. In terms of average power production, shown in

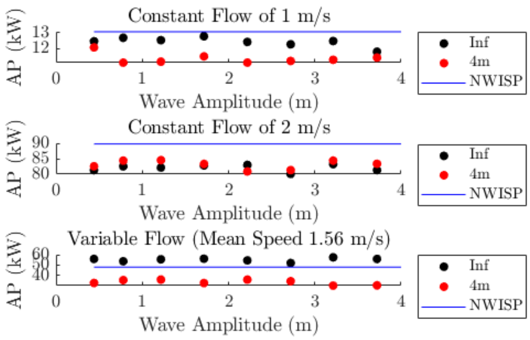

Fig. 11: The above figure depicts the average power production (AP) using the wave parameters from Table IV, for both platform sizes, and the three flow scenarios. Additionally, Inf corresponds to an infinite sized platform, 4m corresponds to the 4m tall platform, and NWISP corresponds to an infinite size platform experiencing no waves ("no waves, infinite sized platform").

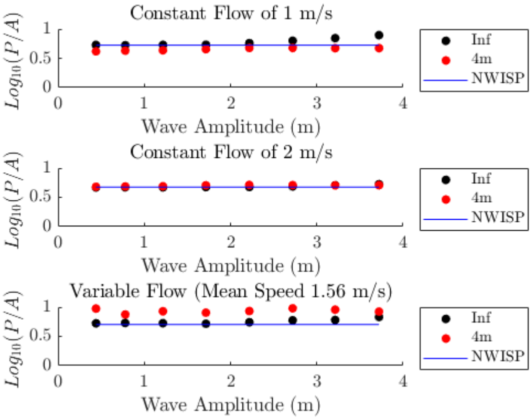

Fig. 12: The above figure depicts the log_{10} of the peak-to-average power ratio ($log_{10}(P/A)$) using the wave parameters from Table IV, for both platform sizes, and the three flow scenarios. Additionally, Inf corresponds to an infinite sized platform, 4m corresponds to the 4m tall platform, and NWISP corresponds to an infinite size platform experiencing no waves ("no waves, infinite sized platform").

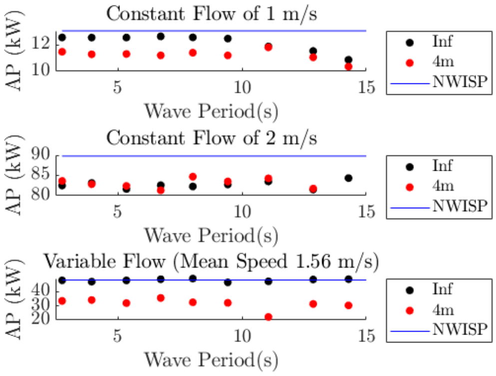

Fig. 13: The above figure depicts the average power production (AP) using the wave parameters from Table V, for both platform sizes, and the three flow scenarios. Additionally, Inf corresponds to an infinite sized platform, 4m corresponds to the 4m tall platform, and NWISP corresponds to an infinite size platform experiencing no waves ("no waves, infinite sized platform").

TABLE V
MOST COMMONLY OCCURRING PEAK PERIODS PER BIN AND THE CORRESPONDING MOST COMMON WAVE HEIGHTS WITHIN THOSE BINS.

$T_p(s)^*$	$H_s(m)$
2.76	0.66
3.95	0.91
5.35	1.14
6.73	1.36
8.02	1.32
9.43	1.36
11.1	1.55
12.9	1.67
14.3	1.85

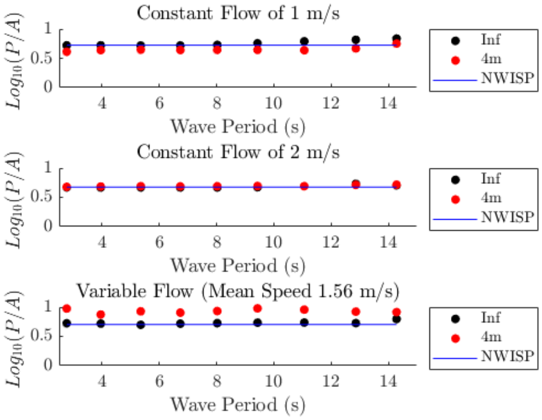

Fig. 14: The above figure depicts the log_{10} of the peak-to-average power ratio ($log_{10}(P/A)$) using the wave parameters from Table V, for both platform sizes, and the three flow scenarios. Additionally, Inf corresponds to an infinite sized platform, 4m corresponds to the 4m tall platform, and NWISP corresponds to an infinite size platform experiencing no waves ("no waves, infinite sized platform").

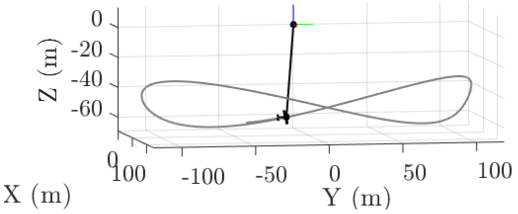

Fig. 15: Depiction of the kite traveling its figure-8 path.

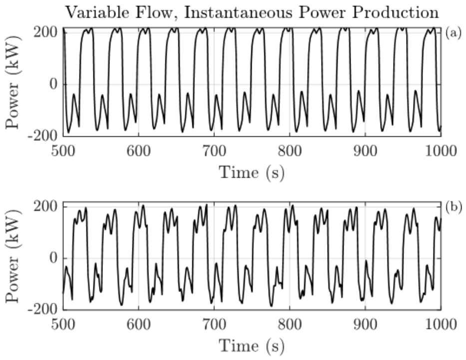

Fig. 16: The above figure depicts the instantaneous power for the kite deployed from (a) an infinite size platform and (b) a 4m tall platform in the turbulent flow with wave effects scenario. The wave parameters in this specific case were a peak period of 9.43 seconds and a significant wave height of 1.36 meters.

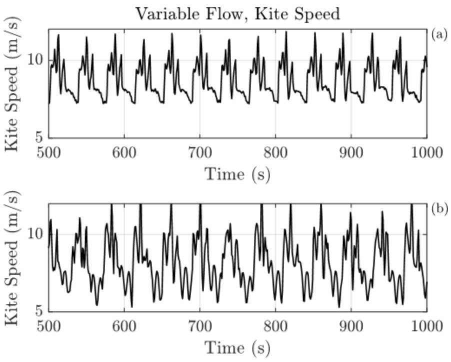

Fig. 17: The above figure depicts the kite's speed when the kite is deployed from (a) an infinite size platform and (b) a 4m tall platform in the turbulent flow with wave effects scenario. The wave parameters in this specific case were a peak period of 9.43 seconds and a significant wave height of 1.36 meters.

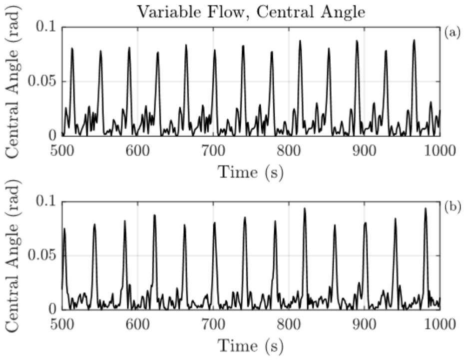

Fig. 18: The above figure depicts the central angle (a measure of tracking error) for the kite deployed from (a) an infinite size platform and (b) a 4m tall platform in the turbulent flow with wave effects scenario. The wave parameters in this specific case were a peak period of 9.43 seconds and a significant wave height of 1.36 meters.

Figs. 11 and 13, the two figures demonstrate that while the average power for each flow scenario and platform size is generally 10-20 percent less than the benchmark performance with no waves and an infinitely-sized platform (NWISP), there was no clear trend of the kite producing less power as wave amplitude and wave period increased. It is apparent that the smaller platform does result in more of a performance degradation than a fixed platform at lower average flow speeds; however, the performance with the smaller floating platform is more closely aligned with the performance under a fixed platform at the higher flow speed of 2 m/s. It is hypothesized that this is because the ratio of the vertical wave velocities to the mean horizontal flow speed is higher at low mean flow speeds, resulting in larger variations in the local angles of attack at the operating depths of the kite. Finally, it is worth noting that the wave periods studied (up to 14 seconds) are far shorter than the periods associated with figure-8 cross-current flight (which are in the 50-100 second range, depending on the prevailing flow speed). Thus, the wave period in isolation is not anticipated to have a significant impact on the kite's periodic power output profile, nor is this seen in the simulation results.

It is also interesting to note that the kite's performance slightly exceeds that of the benchmark constant flow result in the presence of turbulence and a fixed platform. Because power output varies according to the *cube* of the flow speed, the amount of available energy from a flow whose velocity varies around its mean does indeed exceed the amount of energy available from a constant flow (assuming that constant flow speed is equal to the mean speed of the variable flow). Thus, it is indeed possible to harness more energy in the presence of zero-mean turbulence superimposed on top of the base flow field, *if* the kite control system is sufficiently responsive to these turbulent variations. The simulation results suggest that this control system is sufficiently responsive to harness at least some of the available additional energy from turbulence.

In terms of peak-to-average power ratio, shown in Figs. 12 and 14, the performance can be seen to not be significantly impacted by increasing wave parameters when common wave parameters are encountered. For the variable flow scenario, it can be seen that the peak-to-average power ratio is higher for the small platform case. A comparison of the instantaneous power production when the kite is deployed from both the infinite size platform and small platform in the variable flow scenario (turbulent flow with wave effects) can be seen in Fig. 16. The wave parameters in this specific case were a peak period of 9.43 seconds and a significant wave height of 1.36 meters. It can be seen from this figure that the power profile for the small platform case exhibits lower average power production and more variability. This is attributable to an angle of attack that varies (and consequently veers away from its optimal value) as a result of transient variations in the flow direction. Transient operation at sub-optimal angles of attack results in transient reductions in flight speed, as indicated in Fig. 17. While this is true, the controller still tracks the path well under both platform sizing configurations, as seen in Fig. 18. The metric used to quantify the kites deviation from the path, the central angle, is the angle between the kite's position vector and the position vector of the closest point on the path to the kite's location as measured from the origin.

D. Comprehensive Grid Sweep: Results

The simulation results in Section V-C demonstrate significant robustness of the kite's performance over the most common wave height and period values observed from the Oregon Inlet data. In fact, the results from Figs. 11 and 13 suggest that nearly all simulation scenarios resulted in the kite generating at least 80 percent of the lap-averaged power as the constant flow baseline, and some simulations resulted in slightly *more* power than the baseline (especially in the presence of turbulence). Given that these results represent the most commonly occurring conditions, they are very encouraging; however, two important questions follow from these results:

1) If the range of wave conditions is expanded to include less common, but more extreme, conditions, does the kite continue to exhibit robust performance over the full range?

2) If only limited degradation in lap-averaged power output is observed, even in relatively severe conditions, are there other techno-economic performance attributes that experience degradation in more extreme environments?

To answer the aforementioned questions, we turn to a grid study over a large space of wave height and period. In this study, we examine wave heights up to 16 meters (twice as large as those considered in the binned Oregon Inlet data study) and periods up to 20 seconds, focusing on two quantities:

1) Lap-averaged power (as we have considered up to this point);
2) Peak-to-average power.

Because the peak power output dictates the maximum structural load on the kite and the sizing of the power take-off (PTO) system, large values of peak-to-average power over a figure-8 cycle drive up costs.

For a given base flow speed, we wish to assess whether the lap-averaged power and/or peak-to-average power exhibit a significant correlation with respect to the *additional* energy available through waves and turbulence. Analyzing these correlations is complicated, as the kite is impacted by the flow at the kite, along the length of the tether, and (if deployed off of a floating platform) at the surface of the water. However, the relative importance of the flow at each of these locations is not easy to quantify and is dependent on the relative sizing of the floating platform and kite (a smaller platform will intuitively cause near-surface flow patterns to more significantly impact power metrics), the base flow speed, and the level of turbulence. In order to quantify the relative importance, we introduce a quantity referred to as *effective wave energy density*, E_{eff}, which is a weighted average of energy density down to the kite's operating depth, given by:

$$E_{\text{eff}} = \sum_{k=1}^{n_d} w(z(k)) e_w(z(k)), \tag{70}$$

$$e_w(z(k)) = \frac{1}{2}\rho g A_w^2 e^{z(k)K} \tag{71}$$

where 1 to n_d discretizes the depth from the surface to the kite's mean operating depth, $e_w(z(k))$ represents the wave energy density at a depth z, and $w(z(k))$ represents the weight of depth $z(k)$ (which reflects the importance of the flow at that depth in influencing the kite's performance). The basic method of calculating the effective energy density is illustrated in Fig. 19. For each of five base flow conditions and platform sizes, as indicated in Fig. 20, we performed an optimization to determine the weighting functions, $w(z(k))$, that maximized the correlation between the effective energy density and peak/average power.

Examining Fig. 20, it is unsurprisingly the case that with an infinite-sized platform, the flow at the location of the kite is by far the most important factor in dictating peak/average power. On the other hand, for a smaller platform size, the flow at the location of the platform becomes very significant in influencing peak/average power. Finally, in the presence of turbulence, it is noteworthy that flow at the center of the tether becomes important. Figs. 21a, 21b, and 21c show a very strong positive correlation between the (logarithm of) peak-to-average power ratio and the effective wave energy density under all base flow conditions, for an infinite-sized platform (with correlation coefficients of 0.81, 0.87 and .83 respectively). On the other hand, a relatively constant power output can be seen across all base flow conditions in Figs. 22a, 22b, and 22c. It is noteworthy that while the peak/average power exhibits a clear general increase with effective energy density and the average power remains generally consistent, the variability in either metric increases as effective energy increases. These same trends can be seen for a small platform in Figs. 24c and 24d, depicting the (logarithm of) the average power production for the kite when deployed from a small platform in a constant flow speed of 1 and 2 m/s. The relationship between peak-to-average power and effective wave energy has also been evaluated for a small platform in a constant flow speed of 1 and 2 m/s (with correlation coefficients of 0.69 and 0.57 respectively), as shown in Figs. 24a and 24b. For small effective wave energy densities, the peak-to-average power ratio can be seen to be relatively consistent, but at larger values of peak-to-average power ratio, the variability increases.

One final interesting observation, which is especially notable in the presence of an infinite-sized platform without turbulence, is the fact that even the peak/average power ratio remains consistent up to a point, before increasing with respect to effective wave energy density. For an infinite-sized platform with no turbulence, the threshold beyond which peak/average power remains consistent is approximately 200 kJ/m^2, whereas this threshold drops to approximately 50 kJ/m^2 with the smaller platform. Based on these observations, it is interesting to examine the probability mass function (PMF) and corresponding cumulative density function (CDP) of the Oregon Inlet wave data to understand what percentage of wave environments exceed these thresholds. From the PMF and CDF shown in Fig. 23, it can be seen that the wave energy density falls below 60 kJ/m^2 approximately 99 percent of the time. Consequently, the conditions under which peak/average power begins to suffer from increased wave energy density also fall under the category of extreme conditions. Thus, at least for the selected Oregon Inlet location, the characterized kite design exhibits power and peak/average power performance that is highly robust in the presence of typical wave conditions.

VI. CONCLUSIONS

In this paper, a modeling framework was presented for a kite-based marine hydrokinetic (MHK) system, consisting of a six-degree-of-freedom kite, a six-degree-of-freedom floating platform from which the kite is deployed, and a tether model used for the kite's tether and the platform's mooring lines. Additionally, three different ocean environmental models, incorporating

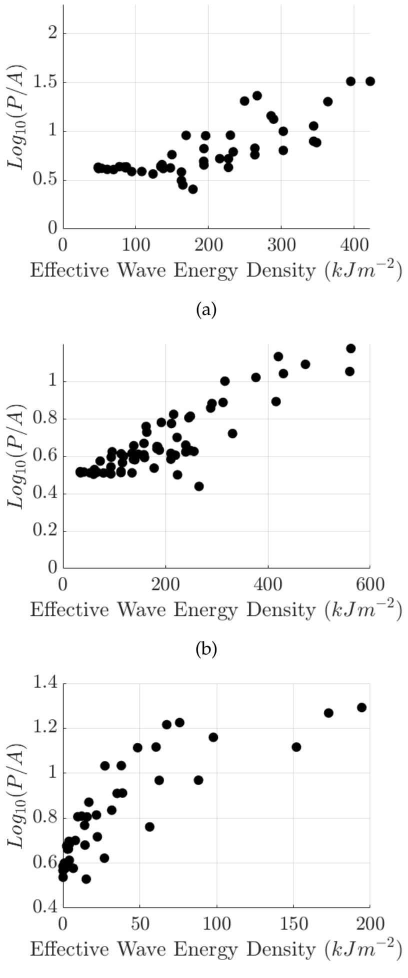

(a)

(b)

(c)

Fig. 21: The logarithm of the peak-to-average power ratio plotted against the effective wave energy density for a kite deployed from the infinite sized platform in waves at (a) a constant flow of 1 m/s, (b) a constant flow of 2 m/s, and (c) in a turbulent flow field.

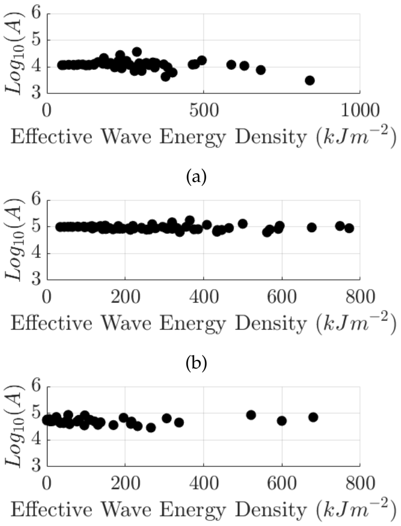

(a)

(b)

(c)

Fig. 22: The logarithm of the average power plotted against the effective wave energy density for a kite deployed from the infinite sized platform in waves at (a) a constant flow of 1 m/s, (b) a constant flow of 2 m/s, and (c) in a turbulent flow field.

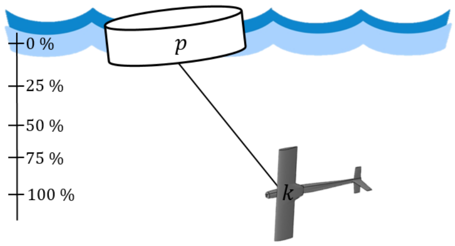

Fig. 19: Depiction of the kite and platform showing the percentage along the depth, which is the y axis of the plot shown in Fig. 20.

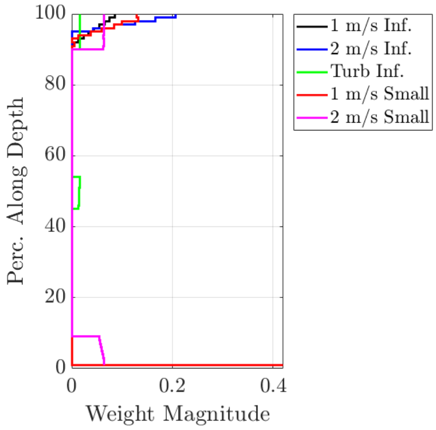

Fig. 20: Depiction of the weight magnitudes given to the wave energy densities at each discretized point in depth from the surface to the kite's mean operating depth, where the weight magnitudes were calculated to maximize the correlation between wave energy density and the peak-to-average power ratio.

realistic wave and turbulence effects, have been presented. For the control of the kite, a hierarchical control framework for kite flight and spooling has been presented, which allows the kite to fly in cyclic, figure-8 paths to generate positive net power. In the results, we show the system performing robustly, both in terms of flight performance and lap-averaged power output, over a full range of wave conditions, in the presence of high-frequency turbulence, and with different platform sizes. Additionally, it has been shown that the lap-averaged power is highly robust to variations in wave height and period, as is peak-to-average power over typical wave conditions. However, peak-to-average power has been shown to be significantly impacted by extreme wave conditions, and to be highly and positively correlated with the effective wave energy density.

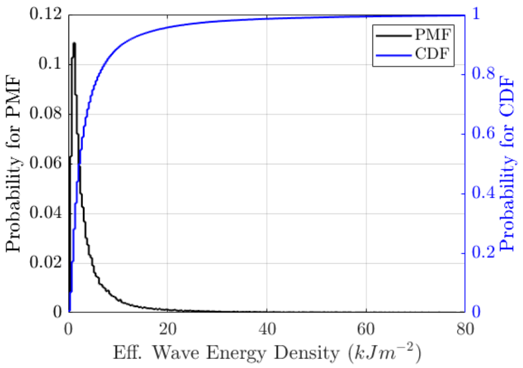

Fig. 23: Probability mass function (PMF) overlaid on top of the cumulative density function (CDF) of effective wave energy density at the CDIP 192 Oregon Inlet Buoy from April 2012 to February 2020.

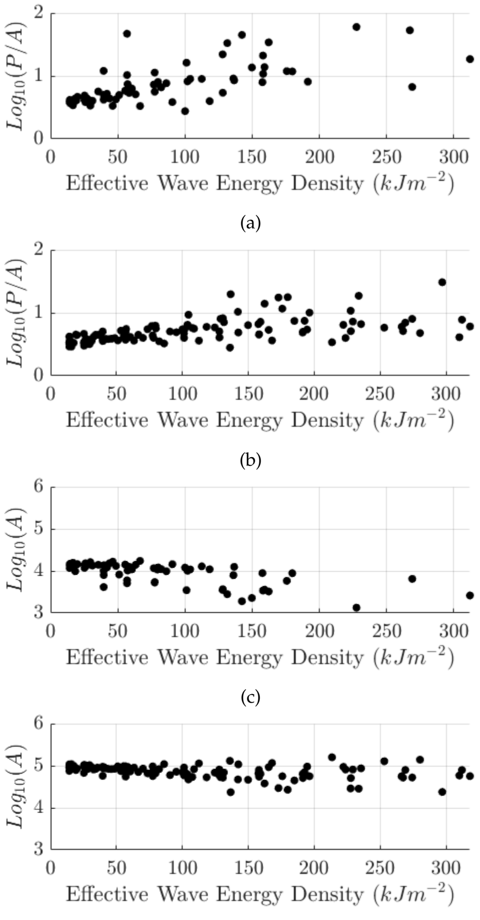

(a)

(b)

(c)

(d)

Fig. 24: The logarithm of the peak-to-average power ratio (a,b) as well as the logarithm of the average power (c,d) plotted against the effective wave energy density for a kite deployed from the small platform in waves at (a,c) a constant flow of 1 m/s, (b,d) a constant flow of 2 m/s.

REFERENCES

[1] P. Jacobson, "Mapping and assessment of the united states ocean wave resource," 2011, electric Power Research Institute (EPRI).

[2] K. A. Haas, H. M. Fritz, S. P. French, B. T. Smith, and V. Neary, "Assessment of energy production potential from tidal streams in the United States," 2011, georgia Tech Research Corporation.

[3] K. A. Haas, H. M. Fritz, S. P. French, and V. Neary, "Assessment of energy production potential from ocean currents along the United States coastline," 2013, georgia Tech Research Corporation.

[4] A. LiVecchi *et al.*, "Powering the blue economy: Exploring opportunities for marine renewable energy in maritime markets," *U.S. Department of Energy*, 2019.

[5] X. Zeng and R. He, "Gulf Stream variability and a triggering mechanism of its meander in the South Atlantic Bight," *Journal of Geophysical Research - Oceans*, vol. 121, 2016.

[6] Minesto, "Minesto, ltd. website," 2019.

[7] A. Ghasemi, D. J. Olinger, and G. Tryggvason, "Computational simulation of the tethered undersea kites for power generation," in *ASME 2015 International Mechanical Engineering Congress and Exposition*. American Society of Mechanical Engineers, 2015, pp. V06BT07A043–V06BT07A043.

[8] M. Loyd, "Crosswind kite power," *Journal of Energy*, vol. 4, no. 3, pp. 106–111, 1980.

[9] Windlift, "Windlift website," 2019.

[10] SkySails, "SkySails power website," 2022. [Online]. Available: https://skysails-power.com/

[11] Kitemill, "Kitemill website," 2022. [Online]. Available: https://www.kitemill.com/

[12] A. Ghasemi, D. J. Olinger, and G. Tryggvason, "A nonlinear computational model of tethered underwater kites for power generation," *Journal of Fluids Engineering*, vol. 138, no. 12, 09 2016. [Online]. Available: https://doi.org/10.1115/1.4034195

[13] D. J. Olinger and Y. Wang, "Hydrokinetic energy harvesting using tethered undersea kites," *Journal of Renewable and Sustainable Energy*, vol. 7, no. 4, p. 043114, 2015.

[14] H. Li, D. J. Olinger, and M. A. Demetriou, "Control of a tethered undersea kite energy system using a six degree of freedom model," in *2015 54th IEEE Conference on Decision and Control (CDC)*. IEEE, 2015, pp. 688–693.

[15] J. Sternberg, J. Goit, S. Gros, J. Meyers, and M. Diehl, "Robust and stable periodic flight of power generating kite systems in a turbulent wind flow field," *IFAC Proceedings Volumes*, vol. 45, no. 25, pp. 140–145, 2012.

[16] U. Fechner and R. Schmehl, "Flight path control of kite power systems in a turbulent wind environment," in *2016 American Control Conference (ACC)*. IEEE, 2016, pp. 4083–4088.

[17] P. Mycek, B. Gaurier, G. Germain, G. Pinon, and E. Rivoalen, "Experimental study of the turbulence intensity effects on marine current turbines behaviour. Part I: One single turbine," *Renewable Energy*, vol. 66, pp. 729–746, 2014.

[18] P. Pyakurel, J. H. VanZwieten, M. Dhanak, and N. I. Xiros, "Numerical modeling of turbulence and its effect on ocean current turbines," *International Journal of Marine Energy*, vol. 17, pp. 84–97, 2017.

[19] J. Reed, M. Cobb, J. Daniels, A. Siddiqui, M. Muglia, and C. Vermillion, "Hierarchical control design and performance assessment of an ocean kite in a turbulent flow environment," in *2020 IFAC World Congress*, 2020.

[20] M. Guérinel, M. Alves, and A. Sarmento, "Nonlinear modelling of the dynamics of a free floating body," *EWTEC, Southampton*, 2011.

[21] F. G. Nielsen, T. D. Hanson, and B. Skaare, "Integrated dynamic analysis of floating offshore wind turbines," in *25th international conference on offshore mechanics and arctic engineering*. American Society of Mechanical Engineers Digital Collection, 2006, pp. 671–679.

[22] X. Chen, Y. Ding, J. Zhang, P. Liagre, J. Niedzwecki, and P. Teigen, "Coupled dynamic analysis of a mini TLP: Comparison with measurements," *Ocean Engineering*, vol. 33, no. 1, pp. 93–117, 2006.

[23] D. Bull and P. Jacob, "Methodology for creating nonaxisymmetric WECs to screen mooring designs using a morison equation approach," in *2012 Oceans*. IEEE, 2012, pp. 1–9.

[24] J. N. Newman, *Marine hydrodynamics*. MIT press, 2018.

[25] UC San Deigo, "Coastal data information program 192 Oregon Inlet buoy," 2020. [Online]. Available: https://cdip.ucsd.edu/themes/cdip/?d2=p70:s:192

[26] US Army Corps of Engineers, "Wave information studies coastal wave hindcast model," 2015. [Online]. Available: http://wis.usace.army.mil/hindcasts.html

[27] J. Reed, J. Daniels, A. Siddiqui, M. Cobb, and C. Vermillion, "Optimal exploration and charging for an autonomous underwater vehicle with energy-harvesting kite," 2019, accepted to American Controls Conference 2020.

[28] C. Vermillion, T. Grunnagle, R. Lim, and I. Kolmanovsky, "Model-based plant design and hierarchical control of a prototype lighter-than-air wind energy system, with experimental flight test results," *IEEE Transactions on Control Systems Technology*, vol. 22, pp. 531–542, 2014.

[29] T. I. Fossen, *Handbook of marine craft hydrodynamics and motion control*. John Wiley & Sons, 2011.

[30] M. Drela and H. Youngren, "AVL," 2017. [Online]. Available: http://web.mit.edu/drela/Public/web/avl/

[31] Z. Yang and A. Copping, *Marine Renewable Energy: Resource Characterization and Physical Effects*. Springer, 2017.

[32] S. Rapp, R. Schmehl, E. Oland, S. Smidt, T. Haas, and J. Meyers, "A modular control architecture for airborne wind energy systems," in *AIAA Scitech 2019 Forum*, 2019, p. 1419.

[33] L. Fagiano, A. U. Zgraggen, M. Morari, and M. Khammash, "Automatic crosswind flight of tethered wings for airborne wind energy: Modeling, control design, and experimental results," *IEEE Transactions on Control Systems Technology*, vol. 22, no. 4, pp. 1433–1447, July 2014.

[34] MathWorks, "Matlab documentation," 2021. [Online]. Available: https://www.mathworks.com/help/index.html?s_tid=CRUX_lftnav